Electromagnetic-Field Theory and Numerically Generated Results for Propagation in Left-Handed Guided-Wave Single-Microstrip Structures

Clifford M. Krowne, *Senior Member, IEEE*

***Abstract*—Dispersion diagrams and magnetic- and electric-field distributions are found for a microstrip structure containing a simple left-handed medium (LHM). The LHM material constituting the substrate has characteristics chosen to overlap with potentially realizable substances. Calculations are done using a fast solver anisotropic Green's function spectral-domain computer code. The theoretical-field method, valid for complex layered structures and anisotropies in the LHM, underlying the computational procedure, which is critical for finding the dispersion diagrams and field distributions, is presented. It is found that the dispersion diagrams and field distributions are very unusual and admit the possibility of completely new device realizations based on combining LHM with conventional materials in a multilayered configuration.**

***Index Terms*—Dispersion diagrams, field distributions, left-handed media (LHM), microstrip.**

I. INTRODUCTION

THERE HAS been great interest in the last few years in trying to understand the properties of structures configured for making focusing devices capable of having radically new properties based on the concepts coming from the use of what has been variously referred to in the literature as negative media, left-handed media, double-negative media, or backward-wave media [1]–[12]. There are many unusual properties of such media and, although in the physics and electronics literature many fascinating issues have been explored, we will not address what has held the attention of most researchers, which are the properties leading to convergent focusing behavior [1], [3] when ordinary media would lead to divergent rays and the attendant perfect focusing consequences. All that will be stated is that in light of multidimensional aspects of real lensing systems, and imperfect media, including finite dispersion and finite loss, the sought-after effect may turn out to be not quite what was expected [5], [11], although still tremendously interesting nevertheless.

Here, no less a fascinating aspect of the left-handed medium (LHM) will be explored, the electronic guiding-wave properties of structures loaded with such media. We choose to define the LHM phenomenologically by assigning to it a negative permittivity $\varepsilon < 0$ and permeability $\mu < 0$ simultaneously satisfied. The slight difference in this definition of an LHM versus, say, using a backward-wave definition, although noticeable, is not enough to confuse the basic phenomenon to follow. Our aim is to first explore the area of dispersion diagram description of a realistic structure for wave propagation, then study some dependencies on the LHM description, and once coming away with some insight of electronic operation, to seek some electromagnetic-field plots to elucidate what might be available in the realm of original devices employing a configuration that yields entirely new distributions of fields.

This is a tall order, and we do not want to overstate our aim. It will be sufficient to merely obtain enough results as outlined above to direct the next effort into understanding where LHM may be useful for integrated circuits. Our study will delve into the microwave and millimeter wavelength regimes. It is expected that the use of LHM in electronic microwave and millimeter-wave devices will allow new types of phase shifters, couplers, and isolators, for example, to be developed. In the first few sections of this paper, we will turn our attention to the transfer P matrix operator theory for field and Green's functions (Section II), electromagnetic-field expressions using the P operators (Section III), and surface current and field extraction formulas (Section IV). Following this, numerically generated dispersion diagrams and electromagnetic-field distributions of single-microstrip structures are presented (Section V).

It is noted here that, in order to keep the approach general and applicable to cases where some of the layers surrounding an LHM layer or the LHM itself have complex material behavior involving anisotropy, bianisotropy, nonreciprocity, or non-Hermiticity [see Fig. 1(a)], the Green's function G and P operators are treated as arising from complex materials.

II. TRANSFER MATRIX OPERATOR FOR FIELDS AND INTERFACIAL GREEN'S FUNCTION

The transfer matrix operator $P(y)$, which takes the tangential fields at one location, say, $y = y_1$, to another location, say, $y = y_2$, is used to both find the interfacial anisotropic Green's function for obtaining the propagation constant and the electric and magnetic fields throughout the device structure [the xy cross section; see the example structure in Fig. 1(a), which

---

Manuscript received April 3, 2003.

The author is with the Microwave Technology Division, Naval Research Laboratory, Washington, DC 20375 USA.

Digital Object Identifier 10.1109/TMTT.2003.819194

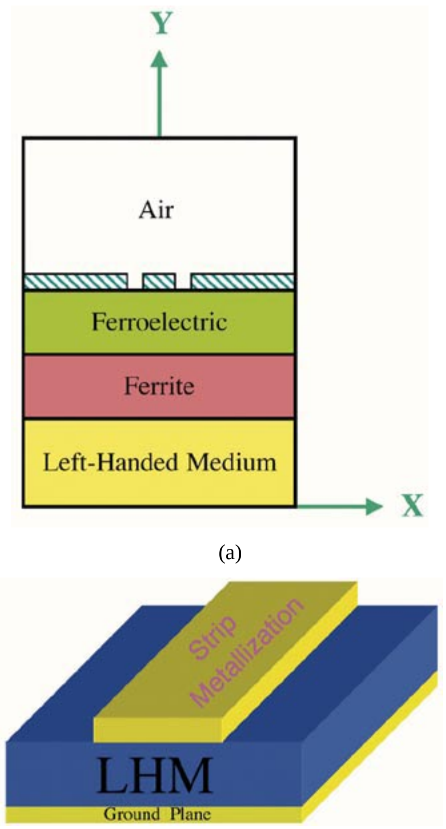

(a)

(b)

Fig. 1. (a) Example structure containing an LHM showing the xy cross section and coordinate axes. (b) Perspective drawing of the single-microstrip structure to be simulated.

shows the coordinate axes with the z-direction pointing out of this paper [13]. It is $P(y) = \exp(Ay)$, where $A = i\omega R$, R being the 4 × 4 matrix describing the material tensor properties of each individual layer and the partial differential Maxwell equations. By the Cayley–Hamilton theorem [14], P may be written as

$$P(y) = \sum_{i=0}^{3} a_i A^i \tag{1}$$

where a_i are the expansion coefficients found by solving a 4 × 4 system, such as the doubly degenerate case

$$\begin{bmatrix} 1 & \gamma_{y1} & \gamma_{y1}^2 & \gamma_{y1}^3 \\ 0 & 1 & 2\gamma_{y1} & 3\gamma_{y1}^2 \\ 1 & \gamma_{y2} & \gamma_{y2}^2 & \gamma_{y2}^3 \\ 0 & 1 & \gamma_{y2} & 3\gamma_{y2}^2 \end{bmatrix} \begin{bmatrix} a_0 \\ a_1 \\ a_2 \\ a_3 \end{bmatrix} = \begin{bmatrix} e^{\gamma_{y1} y} \\ y e^{\gamma_{y1} y} \\ e^{\gamma_{y2} y} \\ y e^{\gamma_{y2} y} \end{bmatrix}. \tag{2}$$

Here, γ_{ym} are the y-directed propagation constants, and may also be viewed as $\gamma_{ym} = \alpha + i\beta = ik_{ym}$. Equation (2) may be stated as

$$S\vec{a} = \vec{v}_r \tag{3}$$

where S is now the matrix operating on the $\vec{a}$ vector resulting in the right-hand vector containing exponential elements $\vec{v}_r$. Some degree of control over the robustness of the numerical solution of (3) occurs by replacing the right-hand-side vector by

$$\vec{v}_r' = \vec{v}_r e^{-\gamma_{ym} y} \tag{4}$$

or

$$\vec{v}_r' = \vec{v}_r e^{-\gamma_{ym} y} = \begin{bmatrix} e^{(\gamma_{y1} - \gamma_{ym}) y} \\ y e^{(\gamma_{y1} - \gamma_{ym}) y} \\ e^{(\gamma_{y2} - \gamma_{ym}) y} \\ y e^{(\gamma_{y2} - \gamma_{ym}) y} \end{bmatrix} \tag{5}$$

yielding an altered $\vec{a}$ vector

$$\vec{a}' = \vec{a} e^{-\gamma_{ym} y}. \tag{6}$$

Operator $P'(y)$ created using the new vector in (6) looks like

$$\begin{aligned} P'(y) &= \sum_{i=0}^{3} a_i' A^i \\ &= \sum_{i=0}^{3} a_i e^{-\gamma_{ym} y} A^i \\ &= e^{-\gamma_{ym} y} \sum_{i=0}^{3} a_i A^i \\ &= e^{-\gamma_{ym} y} P(y). \end{aligned} \tag{7}$$

Next let us examine what this exponential scaling process does to the $P'(y)$ operators needed to make the interfacial anisotropic Green's function for a two-layer structure. The new pull-through operators are

$$\begin{aligned} P'^{(1)} &= P'^{(1)}(h_1) = e^{-\gamma_{ym}^{(1)} h_1} P^{(1)}(h_1) \\ P'^{(2)} &= P'^{(2)}(h_2) = e^{-\gamma_{ym}^{(2)} h_2} P^{(2)}(h_2) \end{aligned} \tag{8}$$

$$P'^{(21)} = P'^{(2)}(h_2) P'^{(1)}(h_1) = e^{-\gamma_{ym}^{(1)} h_1 - \gamma_{ym}^{(2)} h_2} P^{(21)}. \tag{9}$$

Here, h_1 and h_2 are the layer thicknesses for the first and second layers. In general, for the ith layer, its thickness is h_i. For anisotropic Green's functions used in a strip format, the electric fields at the guiding metal interface are related to the surface currents by

$$\begin{aligned} \tilde{E}_x(n) &= \tilde{G}_{xx}(\gamma, n) \tilde{J}_x(n) + \tilde{G}_{xz}(\gamma, n) \tilde{J}_z(n) \\ \tilde{E}_z(n) &= \tilde{G}_{zx}(\gamma, n) \tilde{J}_x(n) + \tilde{G}_{zz}(\gamma, n) \tilde{J}_z(n) \end{aligned} \tag{10}$$

where n indicates the Fourier transform index and the tildas on the symbols indicate Fourier transform variables (a finite Fourier transform is applied). Denoting the ijth element of the pull-through operator P as $P_{ij}^{(r)}$, $r = 1, 2, 21$, anisotropic Green's functions at the interface are

$$\begin{aligned} \tilde{G}_{xx}(\gamma, n) = &\frac{P_{13}^{(1)} \left[P_{24}^{(21)} P_{14}^{(2)} - P_{14}^{(21)} P_{24}^{(2)} \right]}{P_{14}^{(21)} P_{23}^{(21)} - P_{13}^{(21)} P_{24}^{(21)}} \\ &+ \frac{P_{14}^{(1)} \left[P_{13}^{(21)} P_{24}^{(2)} - P_{23}^{(21)} P_{14}^{(2)} \right]}{P_{14}^{(21)} P_{23}^{(21)} - P_{13}^{(21)} P_{24}^{(21)}} \end{aligned} \tag{11}$$

$$\begin{aligned} \tilde{G}_{xz}(\gamma, n) = &-\frac{P_{13}^{(1)} \left[P_{24}^{(21)} P_{13}^{(2)} - P_{14}^{(21)} P_{23}^{(2)} \right]}{P_{14}^{(21)} P_{23}^{(21)} - P_{13}^{(21)} P_{24}^{(21)}} \\ &- \frac{P_{14}^{(1)} \left[P_{13}^{(21)} P_{23}^{(2)} - P_{23}^{(21)} P_{13}^{(2)} \right]}{P_{14}^{(21)} P_{23}^{(21)} - P_{13}^{(21)} P_{24}^{(21)}} \end{aligned} \tag{12}$$

$$\tilde{G}_{zx}(\gamma,n) = \frac{P_{23}^{(1)}\left[P_{24}^{(21)}P_{14}^{(2)} - P_{14}^{(21)}P_{24}^{(2)}\right]}{P_{14}^{(21)}P_{23}^{(21)} - P_{13}^{(21)}P_{24}^{(21)}} + \frac{P_{24}^{(1)}\left[P_{13}^{(21)}P_{24}^{(2)} - P_{23}^{(21)}P_{14}^{(2)}\right]}{P_{14}^{(21)}P_{23}^{(21)} - P_{13}^{(21)}P_{24}^{(21)}} \tag{13}$$

$$\tilde{G}_{zz}(\gamma,n) = -\frac{P_{23}^{(1)}\left[P_{24}^{(21)}P_{13}^{(2)} - P_{14}^{(21)}P_{23}^{(2)}\right]}{P_{14}^{(21)}P_{23}^{(21)} - P_{13}^{(21)}P_{24}^{(21)}} - \frac{P_{24}^{(1)}\left[P_{13}^{(21)}P_{23}^{(2)} - P_{23}^{(21)}P_{13}^{(2)}\right]}{P_{14}^{(21)}P_{23}^{(21)} - P_{13}^{(21)}P_{24}^{(21)}}. \tag{14}$$

Inserting (8) and (9) into (11)–(14), the anisotropic Green's functions may be expressed in terms of the $P'(y)$ operators. Consider the G_{xx} element

$$\begin{aligned}\tilde{G}_{xx}(\gamma,n) &= \frac{e^{\gamma_{ym}^{(1)}h_1}e^{\gamma_{ym}^{(1)}h_1+\gamma_{ym}^{(2)}h_2}e^{\gamma_{ym}^{(2)}h_2}}{e^{\gamma_{ym}^{(1)}h_1+\gamma_{ym}^{(2)}h_2}e^{\gamma_{ym}^{(1)}h_1+\gamma_{ym}^{(2)}h_2}} \\ &\quad\times\left\{\frac{P_{13}^{\prime(1)}\left[P_{24}^{\prime(21)}P_{14}^{\prime(2)} - P_{14}^{\prime(21)}P_{24}^{\prime(2)}\right]}{P_{14}^{\prime(21)}P_{23}^{\prime(21)} - P_{13}^{\prime(21)}P_{24}^{\prime(21)}} + \frac{P_{14}^{\prime(1)}\left[P_{13}^{\prime(21)}P_{24}^{\prime(2)} - P_{23}^{\prime(21)}P_{14}^{\prime(2)}\right]}{P_{14}^{\prime(21)}P_{23}^{\prime(21)} - P_{13}^{\prime(21)}P_{24}^{\prime(21)}}\right\} \\ &= \tilde{G}'_{xx}(\gamma,n).\end{aligned} \tag{15}$$

All other anisotropic Green's function elements give a similar answer, i.e., that the altered anisotropic Green's function and original anisotropic Green's function are identical. This important result leads us to the conclusion that one can do scaling, as shown in (4), without damaging the final interfacial anisotropic Green's function. This reasoning, although somewhat more involved, is applied in Section III for acquiring the electromagnetic fields.

III. ELECTROMAGNETIC FIELDS USING P OPERATORS

Information on the electromagnetic field within a layer and manipulation of the electromagnetic field to effect a transformation of the electromagnetic field from one layer to the next is contained in the column vector

$$\tilde{\Phi}(y) = \begin{bmatrix} \tilde{E}_x \\ \tilde{E}_z \\ \tilde{H}_x \\ \tilde{H}_z \end{bmatrix}. \tag{16}$$

From the fields contained in this field vector, the two other remaining field components $\tilde{E}_y$ and $\tilde{H}_y$ can be found. Using the $P(y)$ operator found in Section II, the fields in the layer under the strips for the two-layer example are

$$\tilde{\Phi}(y) = P^{(1)}(y)\tilde{\Phi}(0) \tag{17}$$

with the field $\tilde{\Phi}(y)$ at the $y = 0$ location for a perfect ground plane given by

$$\tilde{\Phi}(0) = \begin{bmatrix} 0 \\ 0 \\ \tilde{H}_x(0) \\ \tilde{H}_z(0) \end{bmatrix} \tag{18}$$

with

$$\tilde{H}_x(0) = \frac{\tilde{J}_x\left[P_{24}^{(21)}P_{14}^{(2)} - P_{14}^{(21)}P_{24}^{(2)}\right]}{P_{14}^{(21)}P_{23}^{(21)} - P_{13}^{(21)}P_{24}^{(21)}} - \frac{\tilde{J}_z\left[P_{24}^{(21)}P_{13}^{(2)} - P_{14}^{(21)}P_{23}^{(2)}\right]}{P_{14}^{(21)}P_{23}^{(21)} - P_{13}^{(21)}P_{24}^{(21)}} \tag{19}$$

$$\tilde{H}_z(0) = \frac{\tilde{J}_x\left[P_{13}^{(21)}P_{24}^{(2)} - P_{23}^{(21)}P_{14}^{(2)}\right]}{P_{14}^{(21)}P_{23}^{(21)} - P_{13}^{(21)}P_{24}^{(21)}} - \frac{\tilde{J}_z\left[P_{13}^{(21)}P_{23}^{(2)} - P_{23}^{(21)}P_{13}^{(2)}\right]}{P_{14}^{(21)}P_{23}^{(21)} - P_{13}^{(21)}P_{24}^{(21)}}. \tag{20}$$

Currents $\tilde{J}_x$ and $\tilde{J}_z$ are known from the first part of the computational engine, which has found the propagation constant γ along with the unknown expansion coefficients of the surface currents. Note that, throughout this section the first argument of the functions, the spectral index n, is suppressed, while only the coordinate y is retained, to simplify notation. Thus, $\tilde{\Phi}(y)$, $P^{(1)}(y)$, and $\tilde{H}_x(0)$ for example, are actually $\tilde{\Phi}(n,y)$, $P^{(1)}(n,y)$, and $\tilde{H}_x(n,0)$. At the end of Section IV, during the field extraction discussion, the spectral index n or its Fourier transform x is reinstated.

Fields above the interface are expressed by an equation similar to (17) with the discontinuity of the magnetic $\mathbf{H}$ field taken into account. Use of pull-through operators above the interface are necessary [in this case, the only one being $P^{(2)}(y)$].

$$\tilde{\Phi}(y) = P^{(2)}(y)P^{(1)}(h_1)\tilde{\Phi}(0) + P^{(2)}(y)\begin{bmatrix} 0 \\ 0 \\ -\tilde{J}_z \\ \tilde{J}_x \end{bmatrix}. \tag{21}$$

This equation gives the value of the field $\tilde{\Phi}$ in the $i = 2$ layer. Equations (19) and (20) were determined by setting in $\tilde{\Phi}(y) = \tilde{\Phi}(h_T)$ in (21) ($h_T = \sum_{k=1}^{N} h_k$ is the total vertical structure thickness and $N =$ number of layers) and solving the system of equations for $\tilde{H}_x(0)$ and $\tilde{H}_z(0)$ in terms of the surface currents $\tilde{J}_x(0)$ and $\tilde{J}_z(0)$ using the $P(y)$ operators defined by the differential equation

$$\frac{d\tilde{\Phi}(y)}{dy} = i\omega R\tilde{\Phi}(y) \tag{22}$$

with

$$P(y) = e^{i\omega Ry}. \tag{23}$$

Formula (21) is written in global coordinates of the structure, and (22) [and (23)] in local coordinates of the layer. Look at (17) again, rewriting it in the specific coordinate y_i for the ith layer, with $i = 1$ here. Then

$$\tilde{\Phi}_i = \tilde{\Phi}(y_i) = P^{(1)}(y_i)\tilde{\Phi}(0). \tag{24}$$

This equation means that the tangential fields are examined in the ith layer $i = 1$ at the global location $y = y_i$. Since it is the local coordinate that the $P(y)$ operator explicitly operates on, (24) may be recast as

$$\tilde{\Phi}_i = \tilde{\Phi}\left(y'_i\right) = P^{(1)}\left(y'_i\right)\tilde{\Phi}(0) \tag{25}$$

where the local coordinate $y' = y'_i$ now explicitly appears, found as $(h_0 \equiv 0)$

$$y'_i = y_i - \sum_{k=0}^{i-1} h_k \tag{26}$$

from its global structure value y_i by subtracting thicknesses of all the underlying layers.

A general solution of (22) may be stated as

$$\tilde{\Phi}\left(y'_{i2}\right) = P\left(y'_{i2} - y'_{i1}\right)\tilde{\Phi}\left(y'_{i1}\right) \tag{27}$$

for field behavior in the ith layer, where $y'_{i2} > y'_{i1}$. Thus, acquisition of the field $\tilde{\Phi}(y'_{i2})$ further up in the layer at y'_{i2} is accomplished by post-multiplying its value $\tilde{\Phi}(y'_{i1})$ at the lower location y'_{i1} by the pull-up operator $P(y'_{i2} - y'_{i1})$ (multiplication operations occur from right to left). Multiplying both sides of (27) by the inverse of $P(y'_{i2} - y'_{i1})$, assuming it exists, will allow movement from a higher location to a lower one, namely,

$$\begin{aligned}\tilde{\Phi}\left(y'_{i1}\right) &= \left[P\left(y'_{i2} - y'_{i1}\right)\right]^{-1}\tilde{\Phi}(y'_{i2})\\ &= P^{-1}\left(y'_{i2} - y'_{i1}\right)\tilde{\Phi}\left(y'_{i2}\right)\\ &= P\big(-\left[y'_{i2} - y'_{i1}\right]\big)\tilde{\Phi}\left(y'_{i2}\right)\end{aligned} \tag{28}$$

where the last line in (28) follows from (23), meaning the inverse will exist. Operator $P(-[y'_{i2} - y'_{i1}])$ can be written as $P^{(i)}(-\Delta y_i)$, where $\Delta y_i = y'_{i2} - y'_{i1} > 0$ and the subscript notation stores the layer information as before. Therefore, the equivalent of (21) for marching down the structure (decreasing y) is

$$\tilde{\Phi}(y) = \left[P^{(1)}(y)\right]^{-1}\left[P^{(2)}(h_2)\right]^{-1}\tilde{\Phi}(h_T) - \left[P^{(1)}(y)\right]^{-1}\begin{bmatrix}0\\0\\-\tilde{J}_z\\\tilde{J}_x\end{bmatrix} \tag{29}$$

where the reversed sign in the second term arises from not adding on the discontinuity in advancing to larger y, but in subtracting due to reducing y. This equation gives the value of the field $\tilde{\Phi}$ in the $i = 1$ layer.

Instead of using (21) to find $\tilde{\Phi}$ at the top of the structure, (29) can be utilized by setting $\tilde{\Phi}(y) = \tilde{\Phi}(0)$ and solving the system of equations for $\tilde{H}_x(h_T)$ and $\tilde{H}_z(h_T)$ in terms of the surface currents $\tilde{J}_x$ and $\tilde{J}_z$ using the inverse of the $P(y)$ operators. Enlisting the fact that

$$\left[P^{(i)}\left(y'_{i2} - y'_{i1}\right)\right]^{-1} = P^{(i)}\big(-\left[y'_{i2} - y'_{i1}\right]\big) \tag{30}$$

(29) is put in its most convenient form to enable the following solution:

$$\tilde{\Phi}(y) = P^{(1)}(-y)P^{(2)}(-h_2)\tilde{\Phi}(h_T) + P^{(1)}(-y)\begin{bmatrix}0\\0\\\tilde{J}_z\\-\tilde{J}_x\end{bmatrix}. \tag{31}$$

Consequently, fields in layer $i = 2$ can be expressed as

$$\begin{aligned}\tilde{\Phi}\left(y'_i\right) &= P^{(2)}\big(-\left[h_i - y'_i\right]\big)\tilde{\Phi}(h_T)\\ &= P^{(2)}\left(-\left[h_T - y_i - \sum_{k=i+1}^{N} h_k\right]\right)\tilde{\Phi}(h_T).\end{aligned} \tag{32}$$

Here, the first line in (32) uses a local coordinate for the variable argument $P^{(2)}$, the second line uses a global coordinate. The starting top field is

$$\tilde{\Phi}(h_T) = \begin{bmatrix}0\\0\\\tilde{H}_x(h_T)\\\tilde{H}_z(h_T)\end{bmatrix} \tag{33}$$

with

$$\begin{aligned}\tilde{H}_x(h_T) = &-\frac{\tilde{J}_x\left[P_{24}^{(12)}P_{14}^{(1)} - P_{14}^{(12)}P_{24}^{(1)}\right]}{P_{14}^{(12)}P_{23}^{(12)} - P_{13}^{(12)}P_{24}^{(12)}}\\ &+\frac{\tilde{J}_z\left[P_{24}^{(12)}P_{13}^{(1)} - P_{14}^{(12)}P_{23}^{(1)}\right]}{P_{14}^{(12)}P_{23}^{(12)} - P_{13}^{(12)}P_{24}^{(12)}}\end{aligned} \tag{34}$$

$$\begin{aligned}\tilde{H}_z(h_T) = &-\frac{\tilde{J}_x\left[P_{13}^{(12)}P_{24}^{(1)} - P_{23}^{(12)}P_{14}^{(1)}\right]}{P_{14}^{(12)}P_{23}^{(12)} - P_{13}^{(12)}P_{24}^{(12)}}\\ &+\frac{\tilde{J}_z\left[P_{13}^{(12)}P_{23}^{(1)} - P_{23}^{(12)}P_{13}^{(1)}\right]}{P_{14}^{(12)}P_{23}^{(12)} - P_{13}^{(12)}P_{24}^{(12)}}\end{aligned} \tag{35}$$

where all arguments of $P(y)$ operators are understood to be negatives of the respective layer thicknesses, i.e.,

$$P^{(i)} = P^{(i)}(-h_i), \qquad i = 1, 2 \tag{36}$$

$$P^{(12)} = P^{(1)}(-h_1)P^{(2)}(-h_2). \tag{37}$$

Again, as in Section II for the interfacial anisotropic Green's function, a greater degree of control over the robustness of the numerical solution of E and H occurs by taking the diagonal exponential eigenmode matrix in the $P(y)$ construction

$$K^l\left(y'_l\right) = \begin{bmatrix} e^{\gamma_{1l}y'_l} & 0 & 0 & 0\\ 0 & e^{\gamma_{2l}y'_l} & 0 & 0\\ 0 & 0 & e^{\gamma_{3l}y'_l} & 0\\ 0 & 0 & 0 & e^{\gamma_{4l}y'_l}\end{bmatrix} \tag{38}$$

and replacing it by

$$K'^l\left(y'_l\right) = \begin{bmatrix} e^{\gamma_{1l}y'_l-\gamma_{lm}h_l} & 0 & 0 & 0\\ 0 & e^{\gamma_{2l}y'_l-\gamma_{lm}h_l} & 0 & 0\\ 0 & 0 & e^{\gamma_{3l}y'_l-\gamma_{lm}h_l} & 0\\ 0 & 0 & 0 & e^{\gamma_{4l}y'_l-\gamma_{lm}h_l}\end{bmatrix} \tag{39}$$

where in the lth layer

$$P^{(l)}\left(y_l'\right) = \Psi^l(0) K^l\left(y_l'\right)\left[\Psi^l(0)\right]^{-1}. \tag{40}$$

Here, $\Psi^l(0)$ is the 4 × 4 matrix made up of the eigenmode column vectors $\phi_i^l(0)$, $i = 1, 2, 3, 4$

$$\Psi^l(0) = \left[\phi_1^l(0) \quad \phi_3^l(0) \quad \phi_3^l(0) \quad \phi_4^l(0)\right]. \tag{41}$$

Based upon the altered $K^l(y_l')$ from (38) and (39)

$$K'^l\left(y_l'\right) = K^l\left(y_l'\right) e^{-\gamma_{ym}^l h_l} \tag{42}$$

and the altered operator is

$$P'^{(l)}\left(y_l'\right) = P^{(l)}\left(y_l'\right) e^{-\gamma_{ym}^l h_l}. \tag{43}$$

The altered $P(y)$ operators must be placed into the $y = 0$ $\mathbf{H}$ field expressions, suitably generalized from (19) and (20) for any number of layers in the device

$$\begin{aligned}\tilde{H}_x(0) = {} & \frac{\tilde{J}_x\left[P_{24}^{(T_{ab})}P_{14}^{(a)} - P_{14}^{(T_{ab})}P_{24}^{(a)}\right]}{P_{14}^{(T_{ab})}P_{23}^{(T_{ab})} - P_{13}^{(T_{ab})}P_{24}^{(T_{ab})}}\\ & - \frac{\tilde{J}_z\left[P_{24}^{(T_{ab})}P_{13}^{(a)} - P_{14}^{(T_{ab})}P_{23}^{(a)}\right]}{P_{14}^{(T_{ab})}P_{23}^{(T_{ab})} - P_{13}^{(T_{ab})}P_{24}^{(T_{ab})}}\end{aligned} \tag{44}$$

$$\begin{aligned}\tilde{H}_z(0) = {} & \frac{\tilde{J}_x\left[P_{13}^{(T_{ab})}P_{24}^{(a)} - P_{23}^{(T_{ab})}P_{14}^{(a)}\right]}{P_{14}^{(T_{ab})}P_{23}^{(T_{ab})} - P_{13}^{(T_{ab})}P_{24}^{(T_{ab})}}\\ & - \frac{\tilde{J}_z\left[P_{13}^{(T_{ab})}P_{23}^{(a)} - P_{23}^{(T_{ab})}P_{13}^{(a)}\right]}{P_{14}^{(T_{ab})}P_{23}^{(T_{ab})} - P_{13}^{(T_{ab})}P_{24}^{(T_{ab})}}\end{aligned} \tag{45}$$

where

$$\begin{aligned}P^{(T_{ab})} &= \prod_{i=1}^{N} P^{(i)}(h_i)\\ P^{(a)} &= \prod_{i=N_b+1}^{N_a} P^{(i)}(h_i)\\ P^{(b)} &= \prod_{i=1}^{N_b} P^{(i)}(h_i).\end{aligned} \tag{46}$$

In (46), the products advance to the left, with N being the total number of layers, and N_a and N_b being, respectively, the number of layers above and below the interface. Applying (43) to (44) and (45) produces

$$\begin{aligned}\tilde{H}_x'(0) = {} & \frac{\tilde{J}_x\left[P_{24}'^{(T_{ab})}P_{14}'^{(a)} - P_{14}'^{(T_{ab})}P_{24}'^{(a)}\right]}{P_{14}'^{(T_{ab})}P_{23}'^{(T_{ab})} - P_{13}'^{(T_{ab})}P_{24}'^{(T_{ab})}}\\ & - \frac{\tilde{J}_z\left[P_{24}'^{(T_{ab})}P_{13}'^{(a)} - P_{14}'^{(T_{ab})}P_{23}'^{(a)}\right]}{P_{14}'^{(T_{ab})}P_{23}'^{(T_{ab})} - P_{13}'^{(T_{ab})}P_{24}'^{(T_{ab})}}\\ = {} & \left\{\frac{\tilde{J}_x\left[P_{24}^{(T_{ab})}P_{14}^{(a)} - P_{14}^{(T_{ab})}P_{24}^{(a)}\right]}{P_{14}^{(T_{ab})}P_{23}^{(T_{ab})} - P_{13}^{(T_{ab})}P_{24}^{(T_{ab})}}\right.\\ & \left. - \frac{\tilde{J}_z\left[P_{24}^{(T_{ab})}P_{13}^{(a)} - P_{14}^{(T_{ab})}P_{23}^{(a)}\right]}{P_{14}^{(T_{ab})}P_{23}^{(T_{ab})} - P_{13}^{(T_{ab})}P_{24}^{(T_{ab})}}\right\}\\ & \times \frac{\prod_{i=1}^{N} e^{-\gamma_{ym}^i h_i} \prod_{i=N_b+1}^{N} e^{-\gamma_{ym}^i h_i}}{\left[\prod_{i=1}^{N} e^{-\gamma_{ym}^i h_i}\right]^2}\\ = {} & \tilde{H}_x(0) \prod_{i=1}^{N} e^{\gamma_{ym}^i h_i} \prod_{i=N_b+1}^{N} e^{-\gamma_{ym}^i h_i}\\ = {} & \tilde{H}_x(0) \prod_{i=1}^{N_b} e^{\gamma_{ym}^i h_i} \prod_{i=N_b+1}^{N} e^{\gamma_{ym}^i h_i} \prod_{i=N_b+1}^{N} e^{-\gamma_{ym}^i h_i}\\ = {} & \tilde{H}_x(0) \prod_{i=1}^{N_b} e^{\gamma_{ym}^i h_i}\end{aligned} \tag{47}$$

and

$$\tilde{H}_z'(0) = \tilde{H}_z'(0) \prod_{i=1}^{N_b} e^{\gamma_{ym}^i h_i}. \tag{48}$$

Now the fields may be found below the interface, following (17), but upgraded to any number of layers N_b

$$\tilde{\Phi}^{(l)}\left(y_l'\right) = P^{(l)}\left(y_l'\right) \prod_{i=1}^{l-1} P^{(i)}(h_i) \tilde{\Phi}(0) \tag{49}$$

in the lth layer. For the altered problem, $\tilde{\Phi}^{(l)}(y_l')$ becomes

$$\tilde{\Phi}'^{(l)}\left(y_l'\right) = P'^{(l)}\left(y_l'\right) \prod_{i=1}^{l-1} P'^{(i)}(h_i) \tilde{\Phi}'(0) \tag{50}$$

with the altered ground-plane field $\tilde{\Phi}(y)$

$$\tilde{\Phi}'(0) = \tilde{\Phi}(0) \prod_{i=1}^{N_b} e^{\gamma_{ym}^i h_i} \tag{51}$$

Inserting (43) into (50)

$$\begin{aligned}\tilde{\Phi}'^{(l)}\left(y_l'\right) = {} & P^{(l)}\left(y_l'\right) e^{-\gamma_{ym}^l h_l} \left\{\prod_{i=1}^{l-1} P^{(i)}(h_i) e^{-\gamma_{ym}^i h_i}\right\}\\ & \times \tilde{\Phi}(0) \prod_{i=1}^{N_b} e^{\gamma_{ym}^i h_i}\\ = {} & P^{(l)}\left(y_l'\right) \prod_{i=1}^{l-1} P^{(i)}(h_i) \tilde{\Phi}(0) e^{-\gamma_{ym}^l h_l}\\ & \times \prod_{i=1}^{l-1} e^{-\gamma_{ym}^i h_i} \prod_{i=1}^{N_b} e^{\gamma_{ym}^i h_i}\\ = {} & \tilde{\Phi}^{(l)}\left(y_l'\right) e^{-\gamma_{ym}^l h_l} \prod_{i=1}^{l-1} e^{-\gamma_{ym}^i h_i} \prod_{i=1}^{N_b} e^{\gamma_{ym}^i h_i}\\ = {} & \tilde{\Phi}^{(l)}\left(y_l'\right) \prod_{i=1}^{l} e^{-\gamma_{ym}^i h_i} \prod_{i=1}^{N_b} e^{\gamma_{ym}^i h_i}\\ = {} & \tilde{\Phi}^{(l)}\left(y_l'\right) \prod_{i=1}^{l} e^{-\gamma_{ym}^i h_i} \prod_{i=1}^{l} e^{\gamma_{ym}^i h_i} \prod_{i=l+1}^{N_b} e^{\gamma_{ym}^i h_i}\\ = {} & \tilde{\Phi}^{(l)}\left(y_l'\right) \prod_{i=l+1}^{N_b} e^{\gamma_{ym}^i h_i}.\end{aligned} \tag{52}$$

Field quantity $\tilde{\Phi}'^{(l)}(y_l')$ is calculated, and then it must be re-scaled using (52) by

$$\begin{aligned}\tilde{\Phi}^{(l)}\left(y_l'\right) &= \tilde{\Phi}'^{(l)}\left(y_l'\right)\left[\prod_{i=l+1}^{N_b} e^{\gamma_{ym}^i h_i}\right]^{-1} \\ &= \tilde{\Phi}'^{(l)}\left(y_l'\right)\prod_{i=l+1}^{N_b} e^{-\gamma_{ym}^i h_i}. \qquad (53)\end{aligned}$$

For fields above the interface, (34) and (35) are generalized to

$$\begin{aligned}\tilde{H}_x(h_T) = &-\frac{\tilde{J}_x\left[P_{24}^{(T_{ba})}P_{14}^{(b)} - P_{14}^{(T_{ba})}P_{24}^{(b)}\right]}{P_{14}^{(T_{ba})}P_{23}^{(T_{ba})} - P_{13}^{(T_{ba})}P_{24}^{(T_{ba})}} \\ &+ \frac{\tilde{J}_z\left[P_{24}^{(T_{ba})}P_{13}^{(b)} - P_{14}^{(T_{ba})}P_{23}^{(b)}\right]}{P_{14}^{(T_{ba})}P_{23}^{(T_{ba})} - P_{13}^{(T_{ba})}P_{24}^{(T_{ba})}} \qquad (54)\\ \tilde{H}_z(h_T) = &-\frac{\tilde{J}_x\left[P_{13}^{(T_{ba})}P_{24}^{(b)} - P_{23}^{(T_{ba})}P_{14}^{(b)}\right]}{P_{14}^{(T_{ba})}P_{23}^{(T_{ba})} - P_{13}^{(T_{ba})}P_{24}^{(T_{ba})}} \\ &+ \frac{\tilde{J}_z\left[P_{13}^{(T_{ba})}P_{23}^{(b)} - P_{23}^{(T_{ba})}P_{13}^{(b)}\right]}{P_{14}^{(T_{ba})}P_{23}^{(T_{ba})} - P_{13}^{(T_{ba})}P_{24}^{(T_{ba})}} \qquad (55)\end{aligned}$$

where

$$\begin{aligned}P^{(T_{ba})} &= \prod_{i=N}^{1} P^{(i)}(-h_i) \\ P^{(a)} &= \prod_{i=N_a}^{N_b+1} P^{(i)}(-h_i) \\ P^{(b)} &= \prod_{i=N_b}^{1} P^{(i)}(-h_i). \qquad (56)\end{aligned}$$

Thus,

$$\begin{aligned}\tilde{H}_x'(h_T) &= \tilde{H}_x(h_T)\frac{\prod_{i=N}^{1} e^{\gamma_{ym}^i h_i}\prod_{i=N_b}^{1} e^{\gamma_{ym}^i h_i}}{\left[\prod_{i=N}^{1} e^{\gamma_{ym}^i h_i}\right]^2} \\ &= \tilde{H}_x(h_T)\prod_{i=N}^{1} e^{-\gamma_{ym}^i h_i}\prod_{i=N_b}^{1} e^{\gamma_{ym}^i h_i} \\ &= \tilde{H}_x(h_T)\prod_{i=N}^{N_b+1} e^{-\gamma_{ym}^i h_i}\prod_{i=N_b}^{1} e^{-\gamma_{ym}^i h_i}\prod_{i=N_b}^{1} e^{\gamma_{ym}^i h_i} \\ &= \tilde{H}_x(h_T)\prod_{i=N}^{N_b+1} e^{-\gamma_{ym}^i h_i} \qquad (57)\end{aligned}$$

and

$$\tilde{H}_z'(h_T) = \tilde{H}_z'(h_T)\prod_{i=N}^{N_b+1} e^{-\gamma_{ym}^i h_i} \qquad (58)$$

having used a plus sign in the exponent in (43) and the argument of $P^{(l)}$ may be set negative as in (56). Above the interface, the fields are following (32), but upgraded to any number of layers N_a

$$\tilde{\Phi}^{(l)}\left(y_l'\right) = P'^{(l)}\big(-[h_l - y_l']\big)\prod_{i=N}^{l+1} P^{(i)}(-h_i)\tilde{\Phi}(h_T) \qquad (59)$$

in the lth layer. The upper ground-plane field $\tilde{\Phi}(h_T)$ is

$$\tilde{\Phi}'(h_T) = \tilde{\Phi}(h_T)\prod_{i=N}^{N_b+1} e^{-\gamma_{ym}^i h_i}. \qquad (60)$$

Consequently, for the altered problem, $\tilde{\Phi}^{(l)}(y_l')$ becomes

$$\begin{aligned}\tilde{\Phi}'^{(l)}\left(y_l'\right) &= P'^{(l)}\big(-[h_l - y_l']\big)\prod_{i=1}^{l-1} P'^{(i)}(h_i)\tilde{\Phi}'(0) \\ &= P^{(l)}\big(-[h_l - y_l']\big)e^{-\gamma_{ym}^l h_l}\left\{\prod_{i=1}^{l-1} P^{(i)}(h_i)e^{-\gamma_{ym}^i h_i}\right\} \\ &\quad \times \tilde{\Phi}(0)\prod_{i=1}^{N_b} e^{\gamma_{ym}^i h_i} \\ &= P'^{(l)}\big(-[h_l - y_l']\big)\prod_{i=1}^{l-1} P^{(i)}(h_i)\tilde{\Phi}(0)e^{-\gamma_{ym}^l h_l} \\ &\quad \times \prod_{i=1}^{l-1} e^{-\gamma_{ym}^i h_i}\prod_{i=1}^{N_b} e^{\gamma_{ym}^i h_i} \\ &= \tilde{\Phi}^{(l)}\left(y_l'\right)e^{\gamma_{ym}^l h_l}\prod_{i=N}^{l+1} e^{\gamma_{ym}^i h_i}\prod_{i=N}^{N_b+1} e^{-\gamma_{ym}^i h_i} \\ &= \tilde{\Phi}^{(l)}\left(y_l'\right)\prod_{i=N}^{l} e^{\gamma_{ym}^i h_i}\prod_{i=N}^{N_b+1} e^{-\gamma_{ym}^i h_i} \\ &= \tilde{\Phi}^{(l)}\left(y_l'\right)\prod_{i=1}^{l} e^{\gamma_{ym}^i h_i}\prod_{i=N}^{l} e^{\gamma_{ym}^i h_i}\prod_{i=l-1}^{N_b+1} e^{\gamma_{ym}^i h_i} \\ &= \tilde{\Phi}^{(l)}\left(y_l'\right)\prod_{i=l-1}^{N_b+1} e^{\gamma_{ym}^i h_i}. \qquad (61)\end{aligned}$$

Field quantity $\tilde{\Phi}'^{(l)}(y_l')$ is calculated above the interface, and then it must be re-scaled using (61) by

$$\begin{aligned}\tilde{\Phi}^{(l)}\left(y_l'\right) &= \tilde{\Phi}'^{(l)}\left(y_l'\right)\left[\prod_{i=l-1}^{N_b+1} e^{-\gamma_{ym}^i h_i}\right]^{-1} \\ &= \tilde{\Phi}'^{(l)}\left(y_l'\right)\prod_{i=l-1}^{N_b+1} e^{\gamma_{ym}^i h_i}. \qquad (62)\end{aligned}$$

The code finds $\tilde{\Phi}'^{(l)}(y_l')$ and, as the final step, performs (53) or (62). Since $\tilde{\Phi}^{(l)}(y_l') = \tilde{\Phi}^{(l)}(n; y_l')$, a function of the spectral number n, the unscaling is done for each spectral term, noting that $\gamma_{ym}^i = \gamma_{ym}^i(n)$. Acquisition of the Fourier-transformed fields from the spectral-domain processing is the second to last major step in finding the field for producing plots. The final step involves doing the inverse transforms on all the field components, including the current distributions on the strips, which will be covered in Section IV.

IV. SURFACE CURRENTS AND FIELD EXTRACTION

The surface currents can be chosen in a number of ways, it only being necessary to prepare complete sets of basis functions, which are used to construct them. They are selected in the real space domain to display some advantageous property, e.g., edge singularity behavior due to charge repulsion. For the complete set of cosinusoidal basis functions modified by the edge condition, we have for a strip with even-mode symmetry (determined by the z-component symmetry)

$$J_{zm}(x) = \xi_{em}(x) = \begin{cases} \dfrac{\cos\left(\pi \frac{x}{w}[m-1]\right)}{\sqrt{1-\left(\frac{x}{w}\right)^2}}, & |x| \le w \\ 0, \quad w < |x| \end{cases} \tag{63}$$

$$J_{xm}(x) = \eta_{em}(x) = \begin{cases} \dfrac{\sin\left(\pi \frac{x}{w} m\right)}{\sqrt{1-\left(\frac{x}{w}\right)^2}}, & |x| \le w \\ 0, \quad w < |x|. \end{cases} \tag{64}$$

Now let us derive the Fourier transforms of these two current basis functions. We will leave it open as to the polarity of the transform pair used in order to demonstrate an interesting phenomenon, which must be addressed in order to properly align the transform surface currents with their transform electric and magnetic fields. First consider $J_{zm}(x)$, with a transform current for the mth basis function, shown in (65) at the bottom of this page. There are a number of change of variables employed to get the final result, where it is displayed in terms of the Bessel function of the first kind of zeroth order [15].

Next consider $J_{xm}(x)$ with a transform current for the mth basis function, shown in (66) at the bottom of the following page.

What we learn from inspecting (40) and (41) is that the polarity of the Fourier transform will not affect the extraction of the propagation constant γ from the system of equations describing the structure because only the determinant of the system is considered, and signs may be absorbed in expansion coefficients and forgotten. However, reconstruction of the field, including the surface current, requires no uncertainty in polarity of the transform. We choose to use the negative polarity so that the real space current, and electric and magnetic fields given by (**J** in

$$\begin{aligned}
\tilde{\xi}_{em}(n) &= \int_{-\frac{b}{2}}^{\frac{b}{2}} \xi_{em}(x) e^{\pm i\alpha_n x} dx \\
&= \int_{-w}^{w} \frac{\cos\left(\dfrac{\pi x[m-1]}{w}\right)}{\sqrt{1-\left(\dfrac{x}{w}\right)^2}} e^{\pm i\alpha_n x} dx \\
&= \int_{-w}^{w} \frac{\cos(\alpha_n x)\cos\left(\dfrac{\pi x[m-1]}{w}\right)}{\sqrt{1-\left(\dfrac{x}{w}\right)^2}} dx \pm i \int_{-w}^{w} \frac{\sin(\alpha_n x)\cos\left(\dfrac{\pi x[m-1]}{w}\right)}{\sqrt{1-\left(\dfrac{x}{w}\right)^2}} dx \\
&= \frac{1}{2}\int_{-w}^{w} \frac{\left\{\cos\left[\left(\alpha_n + \dfrac{\pi(m-1)}{w}\right)x\right] + \cos\left[\left(\alpha_n - \dfrac{\pi(m-1)}{w}\right)x\right]\right\}}{\sqrt{1-\left(\dfrac{x}{w}\right)^2}} dx \\
&= \int_{0}^{w} \frac{\left\{\cos\left[\left(\alpha_n + \dfrac{\pi(m-1)}{w}\right)x\right] + \cos\left[\left(\alpha_n - \dfrac{\pi(m-1)}{w}\right)x\right]\right\}}{\sqrt{1-\left(\dfrac{x}{w}\right)^2}} dx \\
&= w\int_{0}^{1} \frac{\left\{\cos\left[\left(\alpha_n w + \pi(m-1)\right)x\right] + \cos\left[\left(\alpha_n w - \pi(m-1)\right)x\right]\right\}}{\sqrt{1-x^2}} dx \\
&= w\int_{0}^{1} \frac{\cos\left[\left(\alpha_n w + \pi(m-1)\right)x\right]}{\sqrt{1-x^2}} dx + w\int_{0}^{1} \frac{\cos\left[\left(\alpha_n w - \pi(m-1)\right)x\right]}{\sqrt{1-x^2}} dx \\
&= \frac{\pi w}{2}\left\{J_0\left(\alpha_n w + \pi[m-1]\right) + J_0\left(\alpha_n w - \pi[m-1]\right)\right\}
\end{aligned} \tag{65}$$

$|x| \le w$, may also be found directly from (63) and (64) without the associated Gibbs phenomenon, allowing an extra assessment of the quality of the transform performed)

$$\mathbf{J}(x,y) = \frac{1}{b}\sum_{n=-n_{\max}}^{n_{\max}} \tilde{\mathbf{J}}(n;y)e^{i\alpha_n x} \tag{67}$$

$$\begin{aligned}\mathbf{E}(x,y) &= \frac{1}{b}\sum_{n=-n_{\max}}^{n_{\max}} \tilde{\mathbf{E}}(n;y)e^{i\alpha_n x}\\ \mathbf{H}(x,y) &= \frac{1}{b}\sum_{n=-n_{\max}}^{n_{\max}} \tilde{\mathbf{H}}(n;y)e^{i\alpha_n x}\end{aligned} \tag{68}$$

where the expansion is truncated at a maximum number of terms $n = n_{\max}$ for all field vectors. Basis function maximum expansion numbers $m = m_{\max}$, n_x, and n_z can differ for J_x and J_z in (63) and (64). Currents and fields in (67) and (68) are cross-sectional values, with z-dependence understood as $e^{-\gamma z}$. The current and fields are real physical quantities so they must be converted through

$$\begin{aligned}\mathbf{J}_p(x,y,z) &= \mathrm{Re}\big[\mathbf{J}(x,y)e^{i\omega t-\gamma z}\big]\\ \mathbf{E}_p(x,y,z) &= \mathrm{Re}\big[\mathbf{E}(x,y)e^{i\omega t-\gamma z}\big]\\ \mathbf{H}_p(x,y,z) &= \mathrm{Re}\big[\mathbf{H}(x,y)e^{i\omega t-\gamma z}\big]\end{aligned} \tag{69}$$

which reasserts both the time and z-dependence down the guiding structure. At a particular z-plane, say, $z = 0$, we may drop out the explicit z-dependence, and if we do not wish to watch the time evolution of the harmonic wave, which is sufficient for plotting purposes, we may further set $t = 0$ and write (69) as

$$\begin{aligned}\mathbf{J}_p(x,y) &= \mathrm{Re}\big[\mathbf{J}(x,y)\big]\\ \mathbf{E}_p(x,y) &= \mathrm{Re}\big[\mathbf{E}(x,y)\big]\\ \mathbf{H}_p(x,y) &= \mathrm{Re}\big[\mathbf{H}(x,y)\big].\end{aligned} \tag{70}$$

$$\begin{aligned}\tilde{\eta}_{em}(n) &= \int_{-\frac{b}{2}}^{\frac{b}{2}} \xi_{em}(x)e^{\pm i\alpha_n x}dx\\
&= \int_{-w}^{w} \frac{\sin\left(\frac{\pi x m}{w}\right)}{\sqrt{1-\left(\frac{x}{w}\right)^2}}e^{\pm i\alpha_n x}dx\\
&= \int_{-w}^{w} \frac{\cos(\alpha_n x)\sin\left(\frac{\pi x m}{w}\right)}{\sqrt{1-\left(\frac{x}{w}\right)^2}}dx \pm i\int_{-w}^{w} \frac{\sin(\alpha_n x)\sin\left(\frac{\pi x m}{w}\right)}{\sqrt{1-\left(\frac{x}{w}\right)^2}}dx\\
&= \mp\frac{i}{2}\int_{-w}^{w} \frac{\left\{\cos\left[\left(\alpha_n+\frac{\pi m}{w}\right)x\right]-\cos\left[\left(\alpha_n-\frac{\pi m}{w}\right)x\right]\right\}}{\sqrt{1-\left(\frac{x}{w}\right)^2}}dx\\
&= \mp i\int_{0}^{w} \frac{\left\{\cos\left[\left(\alpha_n+\frac{\pi m}{w}\right)x\right]-\cos\left[\left(\alpha_n-\frac{\pi m}{w}\right)x\right]\right\}}{\sqrt{1-\left(\frac{x}{w}\right)^2}}dx\\
&= \mp iw\int_{0}^{1} \frac{\left\{\cos\left[(\alpha_n w+\pi m)x\right]-\cos\left[(\alpha_n w-\pi m)x\right]\right\}}{\sqrt{1-x^2}}dx\\
&= \mp iw\int_{0}^{1} \frac{\cos\left[(\alpha_n w+\pi m)x\right]}{\sqrt{1-x^2}}dx \pm iw\int_{0}^{1} \frac{\cos\left[(\alpha_n w-\pi m)x\right]}{\sqrt{1-x^2}}dx\\
&= \mp\frac{\pi w}{2}\Big\{J_0(\alpha_n w+\pi m)-J_0(\alpha_n w-\pi m)\Big\}\end{aligned} \tag{66}$$

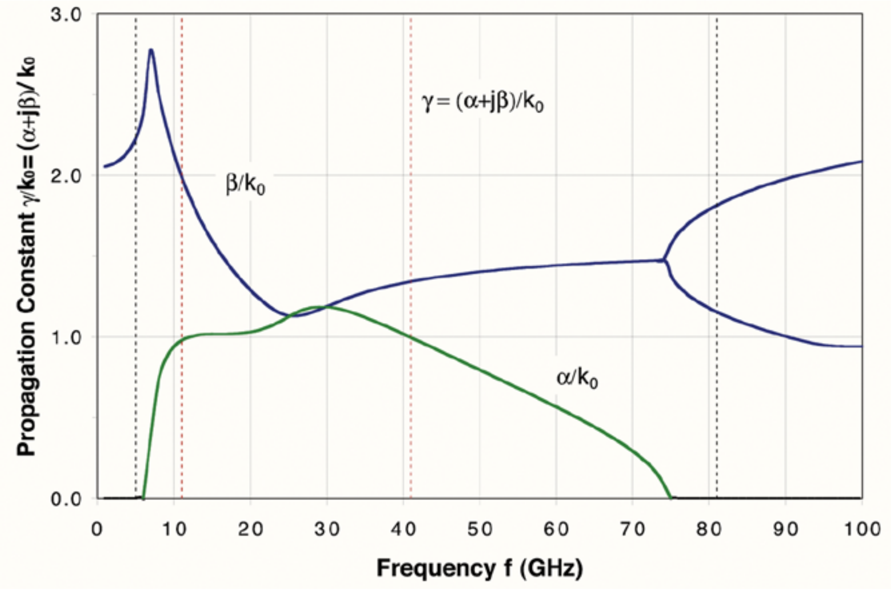

Fig. 2. Dispersion diagram from 1 to 100 GHz for a single-microstrip structure with an LHM substrate. The normalized complex propagation constant $\gamma = (\alpha + j\beta)/k_0$ is shown for only the fundamental even mode. Vertical dashed lines indicate field plots done later in this paper (red) or elsewhere (black).

Finally, the real power flow down the device in the z-direction is found from the instantaneous Poynting vector

$$\mathbf{P}_p(x,y) = \mathbf{E}_p(x,y) \times \mathbf{H}_p(x,y) \tag{71}$$

as

$$\begin{aligned}\mathbf{P}_{pz}(x,y) &= P_{pz}(x,y)\hat{z}\\ &= \left\{\mathbf{E}_p(x,y) \times \mathbf{H}_p(x,y)\right\}_{z \text{ part}}\\ &= \mathbf{E}_{pt}(x,y) \times \mathbf{H}_{pt}(x,y).\end{aligned} \tag{72}$$

The last equality in (72) utilizes transverse fields (cross-sectional fields). The p subscripts are suppressed below since we will only discuss real physical-field distributions.

V. DISPERSION DIAGRAMS

A single-microstrip structure is considered because microstrip is one of the basic building blocks of microwave integrated circuits. Since nothing is known about the characteristics of multilayered microstrip structures utilizing LHMs, we will study the most basic configuration, i.e., a single substrate case. Fig. 1 shows such a structure, which includes the bounding walls (not shown). The strip is presumed perfect metal with width $w_p = 2\ w = 0.5$ mm. Substrate thickness of the LHM is $h_1 = 0.5$ mm, which makes $h_1 = w_p$ for this particular configuration. Symmetrically disposed vertical sidewalls are placed at $x = \pm 2.5$ mm, making the total wall-to-wall separation $b = 5.0$ mm. The second layer above the substrate is selected to be vacuum (ideal air with $\varepsilon = \varepsilon_0 = 1.0$) with thickness $h_2 = 5.0$ mm, making $h_2 = b = 10w = 10h_1$.

Since the absolute values in permittivity $|\varepsilon|$ and permeability $|\mu|$ are nominally in the experimentally frequency band-limited range of 1–10, we choose $\varepsilon = -2.5$ and permeability $\mu = -2.5$ (relative values) as potentially practical values for which simulations would be demonstrative.

Fig. 2 shows the dispersion diagram giving propagation constant $\gamma = (\alpha + j\beta)/k_0$, against the frequency f (in gigahertz). Note that the propagation constant is provided in normalized form, a unitless quantity. This calculation has been done using a spectral-domain simulation employing the moment method with a general Green's function capable of handling arbitrary anisotropy and non-Hermitian media [16]. That is, the tensors describing the materials, in this case, the LHM, could, in fact, be anisotropic and lossy. However, what we have done here is limit ourselves to the situation of isotropy and lossless media, in this case that of the LHM. This will in no way limit our results and insights sought, which will rely on the basic aspects of LHM and Hermiticity. Vertical dashed lines (red) indicate frequency points at which we will later find field distributions or which have been investigated elsewhere (black dashed lines) and are not shown here.

For now, direct attention to the upper (blue) curve giving β and the lower (green) curve giving α. Below 6 GHz and above 75 GHz, only β is nonzero. In these regions, therefore, due to $\alpha = 0$, pure propagation of the wave will occur down the guiding structure in the z-direction. This is not the case for the intermediate region $6 < f < 75$ GHz. Here, $\alpha > 0$, causing the wave to evanesce, a property of a wave traveling that can occur in a medium with a Hermitian constitutive tensor. Examination of the area close to $f = 0$ shows that the slope of $d\beta/df$ becomes gentle while being positive. Thus, one can identify the whole dispersion curve as being associated with a fundamental mode, not unlike that seen for ordinary media substrates, which would limit to a finite β value as $f \rightarrow 0$. Of course, this limiting value is a characteristic of guiding structures with central metal pieces not touching the bounding perfect electric walls.

These bounding electric walls are similar to those found in enclosed structures, and here are, in fact, what may be referred to as computational walls.

Phase velocity is given by $v_p = \omega/\beta = 2\ \pi f/\beta$ and this can be seen to be positive for the entire plotted dispersion curve

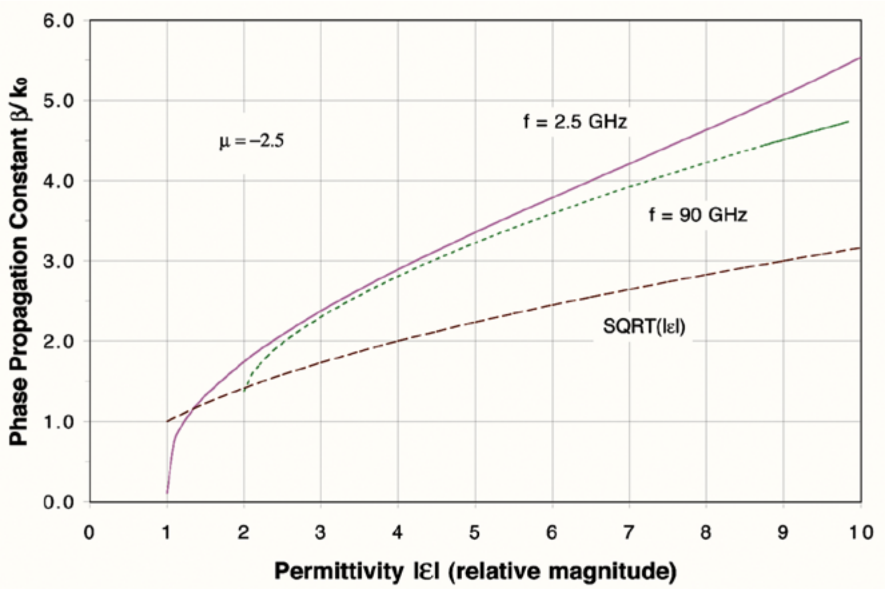

Fig. 3. Phase propagation constant β/k_0 (normalized) versus relative LHM permittivity variation $|\varepsilon|$ over the $|\varepsilon| = 1$–10 range for two frequencies $f = 2.5$ and 90 GHz in the propagating regions of the dispersion diagram. The pure TEM $\sqrt{|\varepsilon|}$ dependence is shown for comparison.

β. However, the story is different for the group velocity $v_g = d\omega/d\,\beta = 2\pi df/d\,\beta = 2\pi/[d\beta/df]$. For the region $6 < f < 26$ GHz, the quantity $d\beta/df < 0$, making $v_g < 0$, while $v_p > 0$, which is to say that with respect to propagation in the z-direction, the wave is a backward wave. Likewise, in the region where $f > 75$ GHz for the lower branch, again, $d\beta/df < 0$, giving us a backward wave in the region where pure phase propagation occurs. This backward-wave behavior neither occurs in the low-frequency regime, however, nor in the upper branch beyond $f = 75$ GHz.

A backward wave will have the power or energy flow per unit time in the opposite direction than the phase propagation [2], [10]. Since the variation of the harmonic spectral solution has a time and z-dependence like $e^{i\omega t - \gamma z}$, which is equal to $e^{i(\omega t - \beta_z)}e^{-\alpha z}$, the vector product $\mathbf{v}_{pl} \cdot \mathbf{v}_{gl}$ sign determines whether or not the wave is backward or not. If $\mathbf{v}_{pl} \cdot \mathbf{v}_{gl} < 0$, the wave is backward. Notice also for the waves that $\alpha > 0$, assuring us that casuality is satisfied. The backwardness of the wave in the transmission (longitudinal) direction z should not be confused with the inherent backwardness (or nearly so with the earlier caveat) of the LHM. This inherent wave backwardness displays itself by acting in the propagation phase $\mathbf{v}_{pt}$ and group $\mathbf{v}_{gt}$ transverse velocities in the xy cross section as they constructively and destructively interfere when waves enter the LHM.

A word should be said about other modal solutions. As the frequency gets higher, generally speaking, more modes seem to become admissible. This is not surprising and not unlike what we are familiar with for ordinary media. Thus, in the higher frequency regime, around 80 GHz, for example, the cluttering of the modal spectrum on a dispersion diagram plot arises. We have purposely left this out in order not to confuse the discussion. Numerical calculations were done using $n_x = n_z = 1$ basis expansion functions for the driving currents on the strip in the x- and z-directions, where the x-direction is in the horizontal direction, the y-coordinate normal to the plane of the layers. Tests were done also for using $n_x = n_z = 5$ and 9. The spectral sum operator in the Fourier-transform domain $\sum_{-n_{\max}}^{n_{\max}}$ has $n_{\max} = 200$, although it too has been looked at for higher $n_{\max} = 400$. Only tiny dependencies were seen on these numerical parameters.

Fig. 3 gives the variation of the phase propagation constant β against the absolute value $|\varepsilon| = -\varepsilon$ of the permittivity. This has been done for two frequencies, each in the regions of pure propagation, $f = 2.5$ GHz and 90 GHz. For small $|\varepsilon|$, the increase is exponential, but it rapidly slows to a linear trend for the upper $f = 2.5$ GHz (magenta) curve and a sub-linear trend for the lower $f = 90$ GHz (green) curve. The upper curve provides β over a 10 : 1 range of permittivity, while the lower curve does this nearly over a 5 : 1 range. The curve showing $\sqrt{|\varepsilon|}$ is provided for reference to TEM guided-wave behavior.

Next we will turn our attention to the electromagnetic-field distributions in Section VI.

VI. ELECTROMAGNETIC-FIELD DISTRIBUTIONS

Once the propagation constant is found, the expansion coefficients used in the driving strip currents may be calculated and, with this determination, the electromagnetic fields are then also found. Since the processing occurs in the spectral domain, the final fields must be mapped back into the real space domain, allowing field distributions to be produced. Figs. 4 and 5 show line plot distributions of the electric $\mathbf{E}_t$ and magnetic $\mathbf{H}_t$ field vectors in the device cross section at 10 GHz. The substrate in Fig. 4 is a regular material and, thus, provides a comparison for the result seen in Fig. 5, which uses an LHM. Line plots are created by proceeding along a field curve in a tangential manner [17] using finite steps Δs, $\Delta s = \sqrt{\Delta x^2 + \Delta y^2}$, which maintain sufficient accuracy to render the final plot representative of the actual field behavior. Fig. 4 was produced using $\Delta s = 0.02$ mm with electric-field lines (solid blue curves) emanating from the microstrip metal and magnetic-field lines (dashed red curves) encircling the strip. The substrate–dielectric interface (here the

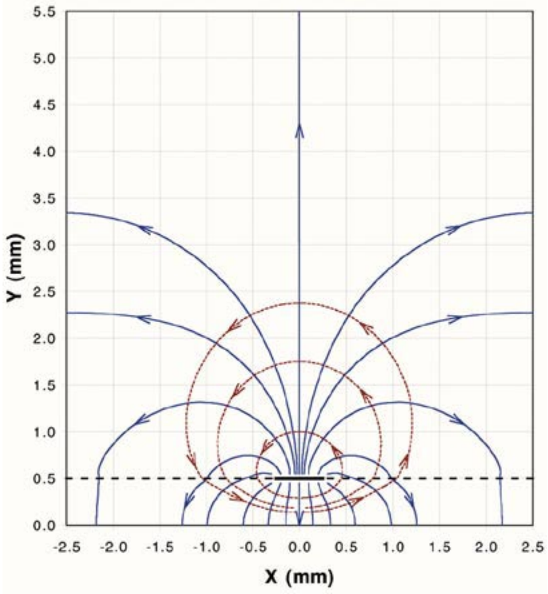

Fig. 4. Line distribution plot of the transverse electric $\mathbf{E}_t$ (solid blue) and magnetic $\mathbf{H}_t$ (dashed red) field vectors in the device cross section at $f = 10$ GHz. The substrate is ordinary material with $\varepsilon = 2.5$ and $\mu = 2.3$, thickness 0.5 mm. Strip width $w_p = 0.5$ mm, air region 5.0-mm high, and structure width $b = 5.0$ mm.

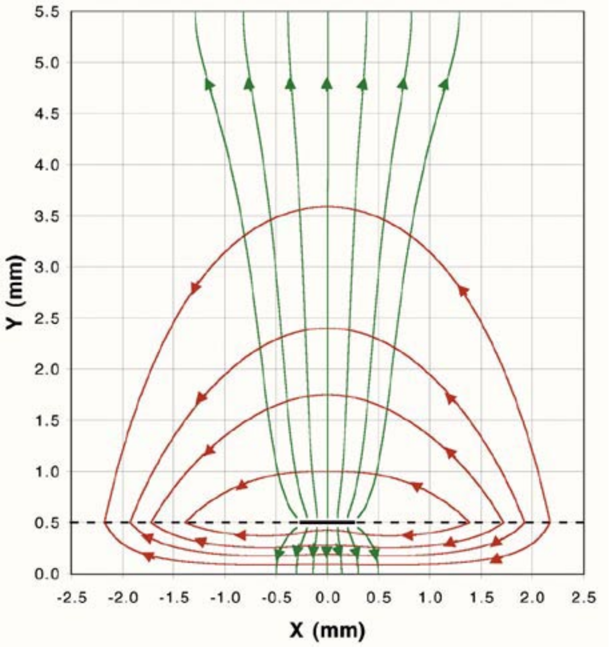

Fig. 5. Line distribution plot of the transverse electric $\mathbf{E}_t$ (solid green) and magnetic $\mathbf{H}_t$ (solid red) field vector directions in the device cross section at $f = 10$ GHz. The substrate is LHM with $\varepsilon = \mu = -2.5$ with the geometry the same as in Fig. 4.

top dielectric is perfect air) is indicated by the black dashed line at $y = 0.5$ mm and the metal itself by the solid black line. Fig. 5 uses $\Delta s = 0.01$ mm with electric (solid green curves) and magnetic (solid red curves) field lines, respectively, again emanating from the microstrip metal and encircling the strip. We are in the complex propagating region of the dispersion diagram (see Fig. 2) near its beginning. It is apparent that the field line distribution is radically altered for the electric fields, with

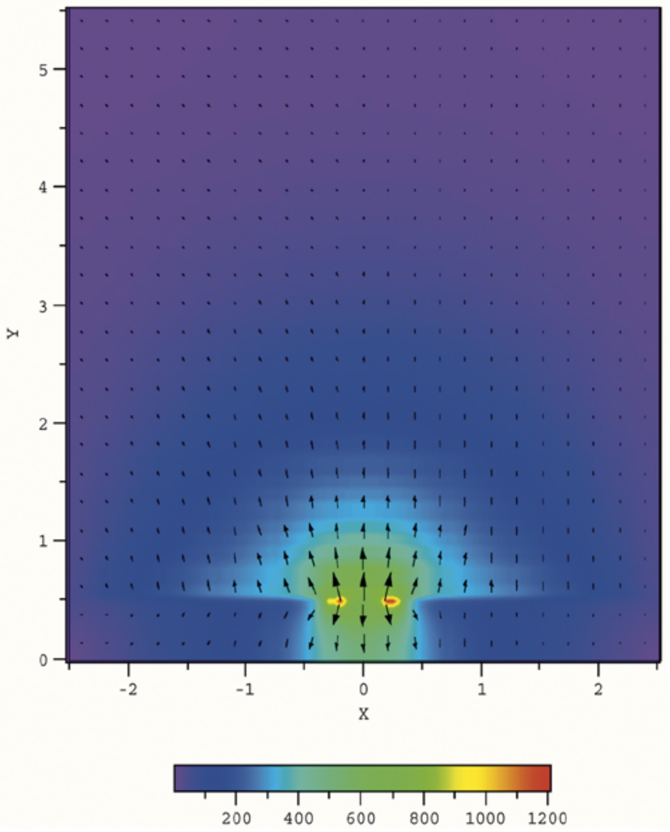

Fig. 6. Field distribution plot of the transverse electric $\mathbf{E}_t$ field vector (arrow length denotes magnitude) overlaid on the electric-field magnitude $E = |\mathbf{E}|$ (color) throughout the LHM device cross section at $f = 10$ GHz. Substrate and geometry are the same as in Fig. 5.

the electric field lines being "repelled" from the interface above the LHM substrate region below. Another surprising result is that the field lines are still pointing away from the strip when going from the normal device in Fig. 4 to the LHM device in Fig. 5. This occurs because the charge distributes such that it is positive on the top microstrip metal surface and negative on the bottom surface. Finally, the magnetic-field lines circulate around the strip, but clockwise below the interface and counterclockwise above it, with their appearance considerably altered from the regular media substrate case. Notice that bilateral symmetry is displayed in Figs. 4 and 5, as expected for scalar materials, whether regular or left-handed.

Although the field line distribution plots are very instructive, they provide more of a qualitative measure, if they do it at all, of the field vector size (relative line density) than a quantitative measure. In order to provide another visualization technique, which can do this directly, Fig. 6 shows both the electric-field magnitude E and the cross-sectional vector field $\mathbf{E}_t$, which with the longitudinal field component E_z generates the total three-dimensional (3-D) vector field $\mathbf{E} = \mathbf{E}_t + \mathbf{E}_z\hat{z}$, where $\hat{z}$ is the unit vector in the z-direction and $\mathbf{E}_t = E_x\hat{x} + E_y\hat{y}$. The plotted E magnitude distribution in Fig. 6 is not the cross-sectional magnitude using only the cross-sectional components of $\mathbf{E}$, but rather the full vector.

All combined arrow and magnitude field plots are generated from a 8372 rectangular grid from the spectral domain code, from which a plotting package Fortner is used to interpolate

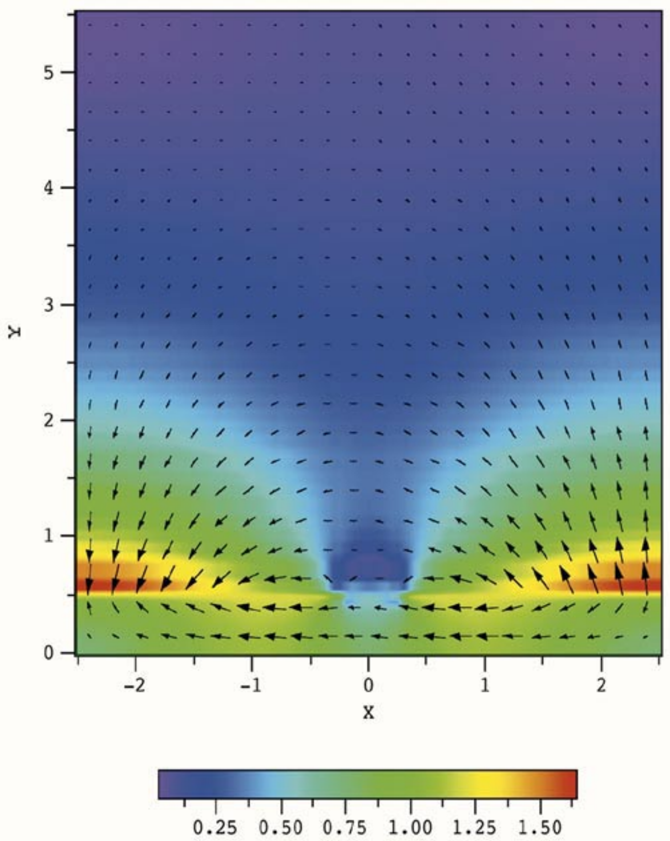

Fig. 7. Field distribution plot of the transverse magnetic $\mathbf{H}_t$ field vector (arrow length denotes magnitude) overlaid on the magnetic-field magnitude $H = |\mathbf{H}|$ (color) throughout the LHM device cross section at $f = 10$ GHz. Substrate and geometry are the same as in Fig. 5.

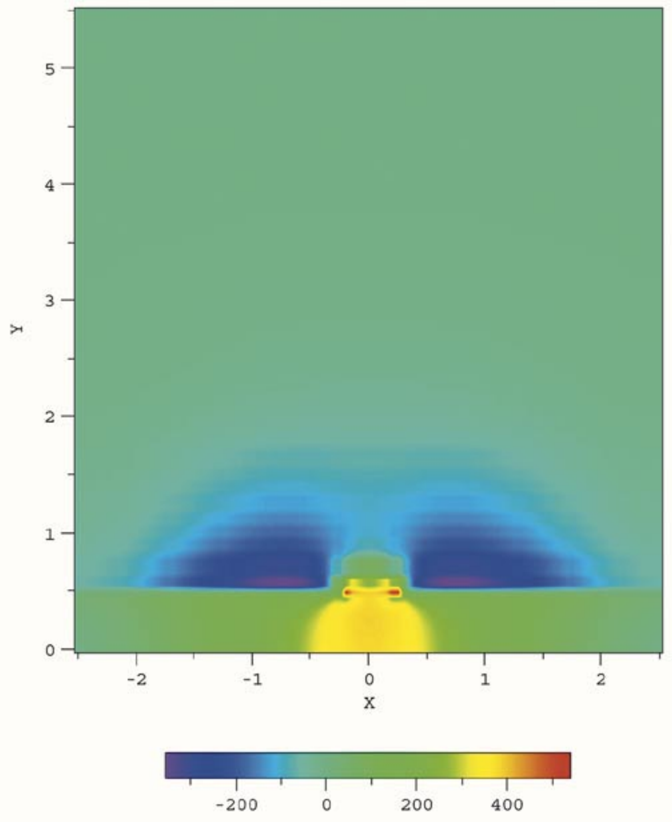

Fig. 8. Field distribution plot of the longitudinal Poynting vector $-\mathbf{P}_z$ field vector (color denotes sign for $\pm z$ and the magnitude) in the LHM device cross section at $f = 10$ GHz. Device dimensions are as in Fig. 5. (Note that we have shown the negative of $\mathbf{P}_z$ based upon the conventions of Fig. 6 and 7.)

for E or H, or produce a 22 × 23 or 23 × 23 grid for $\mathbf{H}_t$ or $\mathbf{E}_t$, respectively. Grid overlays are done by maintaining bilateral symmetry with respect to the y-axis for $\pm x$. (This is why we have ended up with two closely spaced vertical left or horizontal bottom bounding walls, merely an artifact.) The rectangular grid coming out of the spectral-domain code was produced by partitioning each layer vertically into 45 sections and horizontally into 90 sections, for a total of approximately 4000 grid rectangles per layer. Over a decade of field magnitude variation is given by the linear color scale.

Fig. 6 shows that there are local electric vector field behaviors, which display local directional trends on a square grid by square grid basis and interfacial normal and tangential field continuity consistent with the difference in media. Evidence of the unusual interfacial field effects are seen due to the sign switch in the normal component occurring as necessitated by continuous E_x and continuous D_y requirements. Sign switch is imposed by D_y since it is scaled from E_y by the constitutive scalar ε.

Similar to Fig. 6, Fig. 7 shows the magnetic-field magnitude H and the cross-sectional vector field $\mathbf{H}_t$. The overall trend of the magnetic field is to have clockwise circulation in the LHM substrate and reverse or counterclockwise circulation in the overlying region, previously seen in Fig. 5, but vividly shown here. There are also more local vector field behaviors, and interfacial normal and tangential field continuity consistent with the difference in media. Evidence of the unusual interfacial field effects are especially apparent just to the right- and left-hand sides of the strip metal (located at $x = \pm 0.25$ mm) and continuing to the sidewalls, where the sign switch in the normal components occurs necessitated by continuous H_x and continuous B_y requirements. Sign switch is imposed by B_y since it is scaled from H_y by the constitutive scalar μ. This is also seen in the magnetic line curves of Fig. 5.

The last figure completing the assessment at $f = 10$ GHz is the one giving the Poynting vector $\mathbf{P}_z$ for the power propagating down the guiding LHM structure. As seen in Fig. 8, nearly a decade of linear variation is provided in the color scale with the power distribution predominantly flowing in the $-\hat{z}$-direction in the LHM and around the microstrip metal above the substrate. However, some small, but modest sized $+\hat{z}$ flow occurs to either side of the strip in the air region.

Next, the field distribution is studied at $f = 40$ GHz, which is in the middle of the complex propagating region of the dispersion diagram (see Fig. 2). Figs. 9 and 10 give the electric- and magnetic-field arrow-magnitude distributions, respectively (first shown in [18]). Both figures show that the electromagnetic-field distributions are now much more complex than at 10 GHz, and this is not surprising since frequency has been increased by a factor of four, which, among other things, reduces the wavelength accordingly. Also, the fields appear much more localized about the microstrip metal. In order to allow interpretation of these more complex field patterns, line field distributions for electric and magnetic fields have been made

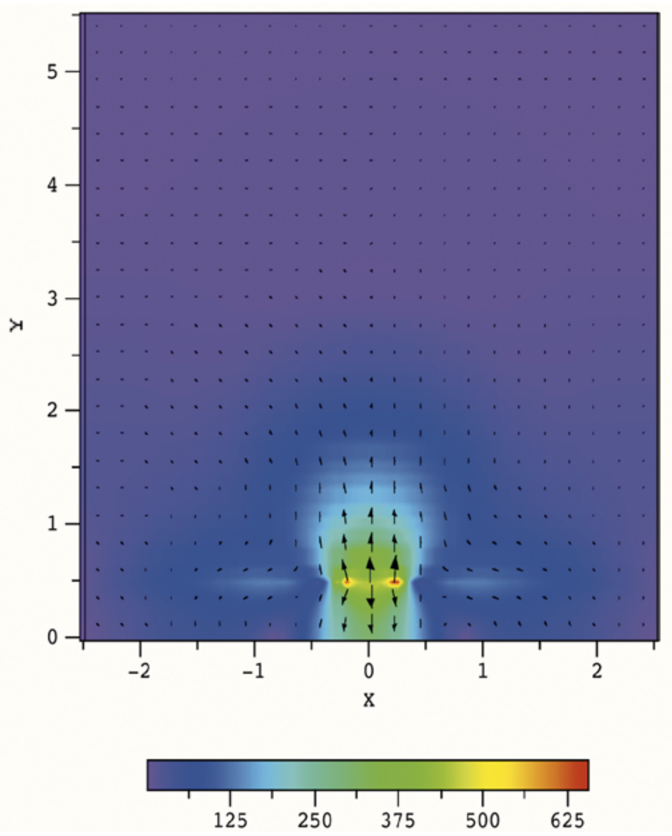

Fig. 9. Field distribution plot of the transverse electric $\mathbf{E}_t$ field vector (arrow length denotes magnitude) overlaid on the electric-field magnitude $E = |\mathbf{E}|$ (color) throughout the LHM device cross section at $f = 40$ GHz. Substrate and geometry are the same as in Fig. 5.

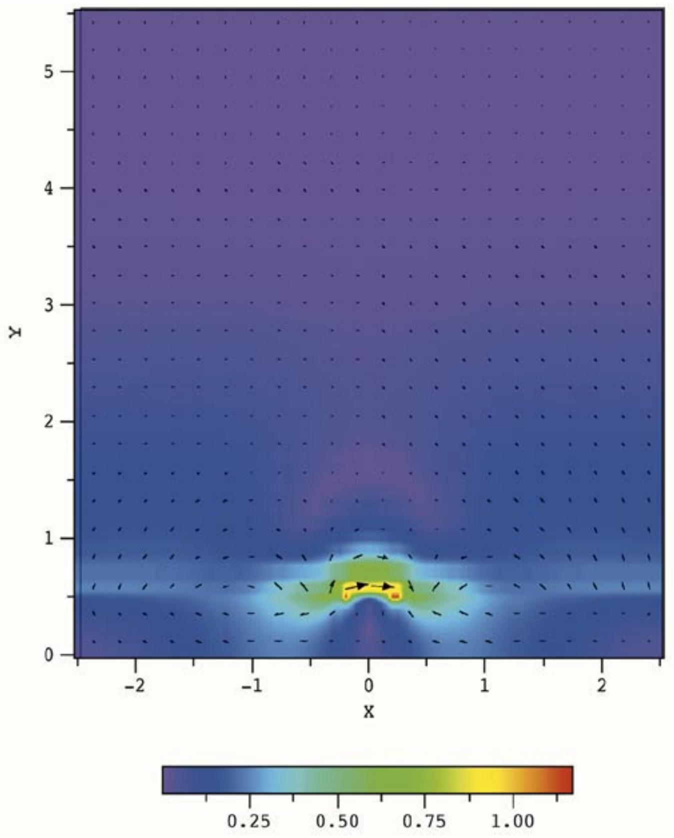

Fig. 10. Field distribution plot of the transverse magnetic $\mathbf{H}_t$ field vector (arrow length denotes magnitude) overlaid on the magnetic-field magnitude $H = |\mathbf{H}|$ (color) throughout the LHM device cross section at $f = 40$ GHz. Substrate and geometry are the same as in Fig. 5.

and overlaid on their respective electric and magnetic magnitude distributions, as shown in Figs. 11 and 12 (color magnitude scales are those used in Figs. 9 and 10). For the electric-field case, all the lines were also redone using $n_x = n_z = 6$ and $n_{\max} = 600$ ($n_x = n_z = 1$ and $n_{\max} = 200$ is the baseline setting) to see what the effect was on the lines and to examine the accuracy of the interfacial conditions. It was found that only very slight or minuscule changes occurred, mostly not even noticeable, with the largest visually apparent change happening for two lines terminating at $y = \pm 2.5$ mm at the place where bending to go vertical occurs above the interface.

Three locations in Fig. 11 are shown where electric arrows butt up against each other, oppositely directed. This occurs at $y = 3.4$ mm, $x = 0$ and $y = 0.47$ mm, $x = \pm 2.08$ mm. In each case, this switch is allowed to occur inside the layer because the field goes to zero precisely at the meeting place of the arrows. For the case in the top region, it is clear what this means in relation to the other electric field lines to either side of the y-axis. However, the effect is a bit more subtle below the interface and is required to maintain the viability of the interfacial boundary conditions. Regarding the numerical quality of the satisfaction of these conditions, it has been found that it is generally within a few percent or better at the regular-LHM boundary and, depending upon the ability to dial in close to the interface and resolve the fields, and varying the basis function numbers and the maximum spectral index, it is not uncommon to see this number reach small fractions of one-hundredth of a percent.

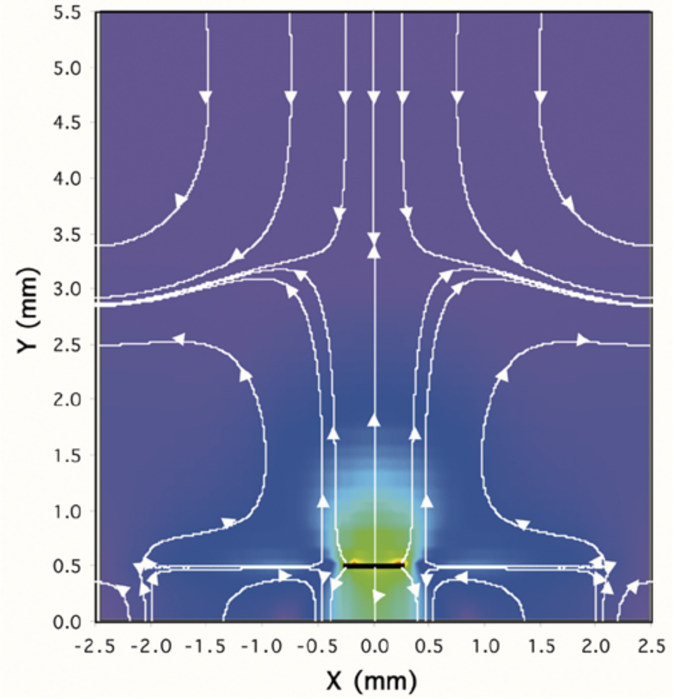

Fig. 11. Line distribution plot of the transverse electric $\mathbf{E}_t$ (solid white) field vector overlaid on the electric-field magnitude $E = |\mathbf{E}|$ (color) in the LHM device cross section at $f = 40$ GHz. Substrate and geometry are the same as in Fig. 5.

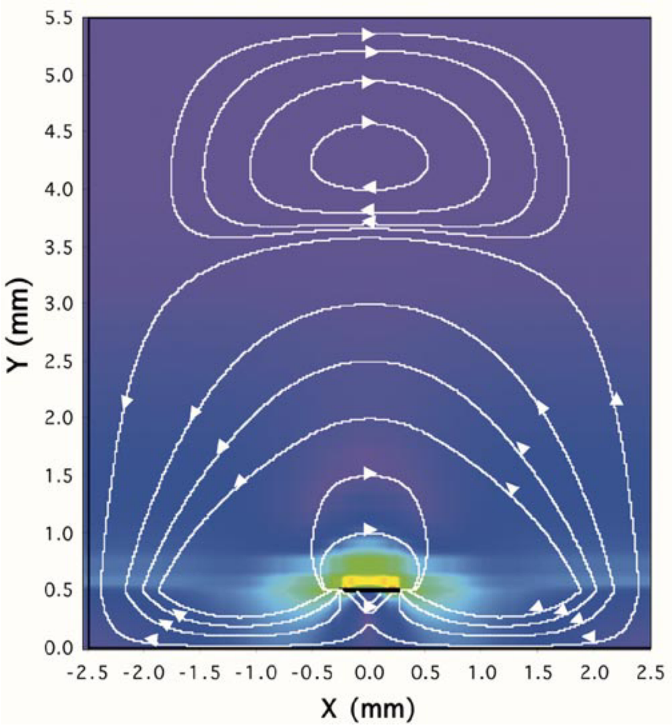

Fig. 12. Line distribution plot of the transverse magnetic $\mathbf{H}_t$ (solid white) field vector overlaid on the magnetic-field magnitude $H = |\mathbf{H}|$ (color) in the LHM device cross section at $f = 40$ GHz. Substrate and geometry are the same as in Fig. 5.

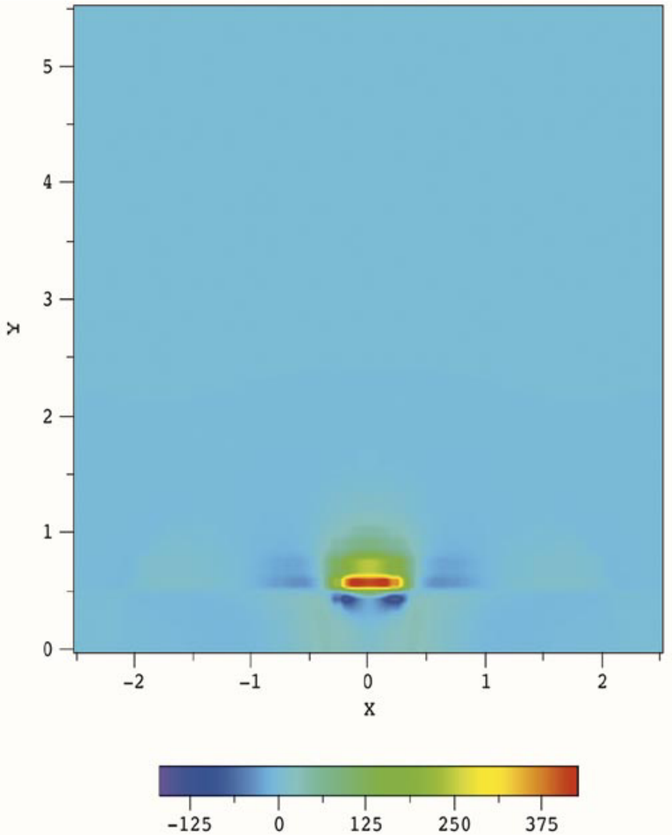

Fig. 13. Field distribution plot of the longitudinal Poynting vector $-\mathbf{P}_z$ field vector (color denotes sign for $\pm z$ and the magnitude) in the LHM device cross section at $f = 40$ GHz. Device dimensions are as in Fig. 5. (Note that we have shown the negative of $\mathbf{P}_z$ based upon the conventions of Fig. 9 and 10.)

Both Figs. 11 and 12 have the microstrip metal indicated by a black line just to help understand where it is located, but the interface has not been marked to avoid obscuring the graphic. It should be remembered that the metal is taken as perfect and of vanishingly small extent in the y-direction. What has changed in the Fig. 12, 40-GHz plot of the magnetic field from that of Fig. 5, 10-GHz plot in terms of field lines, is that we now see three different zones of circulating fields. Firstly, close in to the microstrip metal are clockwise circulating patterns in the top region, which close their loops extremely close to the metal, either just above or below it, obeying the law that the circulations enclose the proper amount of strip and electric displacement currents normal to the cross section. In the same close-in region are counterclockwise circulating fields in the LHM, which close their loops extremely close to the metal again, once again obeying the enclosure rule. The second zone, includes those circulating fields that are counterclockwise above the interface and clockwise below it, going deep into the top layer to a maximum of approximately $y = 3.5$ mm, and reaching to the floor of the LHM layer near $y = 0$ in parts of their curves. Reducing their maximum extent $y_{\max}$ from the 3.5-mm value seems to make the lines land near the microstrip metal edge. The third zone is in the 2×4 mm^2 rectangle beyond $y = 3.5$ mm where the fields circulate clockwise, satisfying the enclosing rule for electric displacement currents. The extent of this final region is not inconsistent with the $\lambda/2$ value in air, 3.75 mm, for filling a simple waveguide (devoid of an exciting strip with delta function located currents). Finally, in Fig. 13, a comparison with Fig. 8 shows that the Poynting vector $\mathbf{P}_z$ has collapsed about the microstrip metal with much of the $-\hat{z}$ directed power flow being taken up by the region above the interface, and the remaining lesser amount of reversed flow just below the metal strip.

Field distributions have been calculated at 5 and 80 GHz also, but space does not enable us to show them here. (For distributions at 5 GHz, see [19][1].) What is learned from all these electromagnetic-field distributions is that the disposition of the fields are radically different from that seen when ordinary media substrates are employed. Although not entirely unexpected, what is surprising are the specific attributes caused by utilizing LHM.

VII. CONCLUSIONS

In this paper, we have determined the dispersion diagrams for a microstrip structure loaded with left-handed media. These diagrams are quite unlike those for ordinary substrates, and open up the possibility of designing entirely new electronic devices. Further support and understanding comes with determining the electromagnetic-field distributions, and we have shown some here. There are still other ways of displaying the electromagnetic behavior in distributions (not shown here), and we have been exploring these in order to ascertain the surprising and sometimes astonishing characteristics of guided-wave structures employing LHM. This area of research is just in its infancy in terms of looking at what such materials

---

[1] In (2) and (3), typos require $\varepsilon_{\rm top}$ and $\varepsilon_{\rm LHM}$ to be replaced by $\varepsilon'_{\rm top} = 1/\varepsilon_{\rm top}$ and $\varepsilon'_{\rm LHM} = 1/\varepsilon_{\rm LHM}$. This makes the electric equation (3) and the later magnetic equation (9) analogous in form. Also, Fig. 5 shows the Poynting vector—$P_{\rm guide}$, not $P_{\rm guide}$.

could do for microwave and millimeter-wave integrated circuits and we expect many more interesting results to follow.

ACKNOWLEDGMENT

The author wishes to thank M. Daniel, DCS Corporation, Alexandria, VA, for software assistance.

REFERENCES

[1] R. W. Ziolkowski and S. Heyman, "Wave propagation in media having negative permittivity and permeability," *Phys. Rev. E, Stat. Phys. Plasmas Fluids Relat. Interdiscip. Top.*, vol. 64, pp. 056 625-1–056 625-15, 2001.

[2] I. V. Lindell, S. A. Tretyakov, K. I. Nikoskinen, and S. IIvonen, "BW media—Media with negative parameters, capable of supporting backward waves," *Microwave Opt. Technol. Lett.*, vol. 31, pp. 129–133, Oct. 2001.

[3] C. Luo, S. G. Johnson, and J. D. Joannopoulos, "All-angle negative refraction in a three-dimensionally periodic photonic crystal," *Appl. Phys. Lett.*, vol. 81, pp. 2352–2354, Sept. 2002.

[4] D. R. Fredkin and A. Ron, "Effectively left-handed (negative index) composite material," *Appl. Phys. Lett.*, vol. 81, pp. 1753–1755, Sept. 2002.

[5] R. M. Walser, A. P. Valanu, and P. M. Valanju, "Comment on extremely low frequency plasmons in metallic mesostructures," *Phys. Rev. Lett.*, vol. 87, p. 119 701-1, Sept. 2001.

[6] M. Notomi, "Theory of light propagation in strongly modulated photonic crystals: Refractionlike behavior in the vicinity of the photonic band gap," *Phys. Rev. B, Condens. Matter*, vol. 62, pp. 10 696–10 705, Oct. 2000.

[7] D. R. Smith, D. C. Vier, W. Padilla, S. C. Nemat-Nasser, and S. Schultz, "Loop-wire medium for investigating plasmons at microwave frequencies," *Appl. Phys. Lett.*, vol. 75, pp. 1425–1427, Sept. 1999.

[8] D. R. Smith, S. Schultz, N. Kroll, M. Sigalas, K. M. Ho, and C. M. Soukoulis, "Experimental and theoretical results for a two-dimensional metal photonic band-gap cavity," *Appl. Phys. Lett.*, vol. 65, pp. 645–647, Aug. 1994.

[9] J. Gerardin and A. Lakhtakia, "Negative index of refraction and distributed Bragg reflectors," *Microwave Opt. Technol. Lett.*, vol. 34, pp. 409–411, Sept. 2002.

[10] M. W. McCall, A. Lakhtakia, and W. S. Weiglhofer, "The negative index of refraction demystified," *Eur. J. Phys.*, vol. 23, pp. 353–359, 2002.

[11] A. L. Pokrovsky and A. L. Efros, "Electrodynamics of metallic photonic crystals and the problem of left-handed materials," *Phys. Rev. Lett.*, vol. 89, pp. 093 901-1–093 901-4, Aug. 2002.

[12] A. Lakhtakia, "An electromagnetic trinity from negative permittivity and negative permeability," *Int. J. Infrared Millim. Waves*, vol. 23, pp. 813–818, June 2002.

[13] C. M. Krowne, "Fourier transformed matrix method of finding propagation characteristics of complex anisotropic layered media," *IEEE Trans. Microwave Theory Tech.*, vol. MTT-32, pp. 1617–1625, Dec. 1984.

[14] T. E. Fortmann and K. L. Hitz, *An Introduction to Linear Control Systems*. New York: Marcel Dekker, 1977.

[15] I. S. Gradshteyn and I. M. Ryzhik, *Table of Integrals, Series, and Products*. San Diego, CA: Academic, 1980.

[16] C. M. Krowne, "Dyadic Green's function modifications for obtaining attenuation in microstrip transmission layered structures with complex media," *IEEE Trans. Microwave Theory Tech.*, vol. 50, pp. 112–122, Jan. 2002.

[17] A. A. Mostafa, C. M. Krowne, K. A. Zaki, and S. Tantawi, "Hybrid-mode fields in isotropic and anisotropic planar microstrip structures," *J. Electromagn. Waves Applicat.*, vol. 5, pp. 577–606, 1991.

[18] C. M. Krowne and M. Daniel, "Electronic aspects of propagation in left-handed guided wave structures: Electromagnetic-media interactions," in *IEEE MTT-S Int. Microwave Symp. Dig.*, June 2003, pp. 309–312.

[19] C. M. Krowne, "Physics of propagation in left-handed guided wave structures at microwave and millimeter wave frequencies," Cornell Univ. Archive, Ithaca, NY, vol. Gen. Phys. 0305004, May 2003.

Clifford M. Krowne (S'73–M'74–SM'83) received the B.S. degree in physics from the University of California at Berkeley and Davis, in 1970, and the M.S. degree and Ph.D. degree (solid-state transport, many body scattering) from the University of California at Los Angeles, in 1972 and 1975, respectively.

He was with the Microelectronics Division, Lockheed Missiles and Space Company, Sunnyvale, CA. He previously worked as a Member of the Solid-State Technical Staff of the Watkins-Johnson Company, Palo Alto, CA. He once was a faculty member with the Department of Electrical Engineering, North Carolina State University, Raleigh. He was also an Adjunct Professor of electrical engineering with the University of Maryland at College Park. Since 1982, he has been with the Microwave Technology Branch, Electronics Science and Technology Division, Naval Research Laboratory, Washington, DC, where he has been involved in the study of microwave and millimeter-wave properties of active and passive solid-state devices. He has authored or coauthored 170 conference and journal papers in solid-state electronics, microwave circuits, electromagnetics, and physics. He holds several patents. He has also authored major portions of four books in the Advances in Imaging and Electron Physics Series on propagation in anisotropic media and circulation behavior in nonreciprocating media (New York: Academic, 1995, vol. 92; 1996, vol. 98; 1998, vol. 103; 1999, vol. 106), and has also made a contribution on numerical modeling of microstrip circulators in the ferrite devices area for the *Electrical and Electronics Engineering Encyclopedia* (New York: Wiley, 1999). He is listed in *Who's Who in Frontiers of Science and Technology*, *Who's Who in the World*, and *Who's Who in Electromagnetics*.

Dr. Krowne is a member of Phi Kappa Phi, Tau Beta Pi, and the American Physical Society. He is a Fellow of the Washington Academy of Sciences (elected 1992). He has served on the Technical Program Conference Committees of the IEEE Antennas and Propagation Society (IEEE AP-S) (1983, 1984) and the IEEE Microwave Theory and Techniques Society (IEEE MTT-S) (1982–1996). He has chaired sessions in the electromagnetic theory, microstrip antenna, and solid-state devices/circuits, superconductor, and monolithic circuit areas, and has organized two IEEE MTT-S workshops on two-dimensional (2-D)/3-D full-wave simulation (1992) and self-consistent particle transport/full-wave dynamic field simulation (1993). He was a member of the 1987 IEEE MTT-S Symposium Steering Committee.